Materialia 20 (2021) 101225

Contents lists available at ScienceDirect

Materialia

journal homepage: www.elsevier.com/locate/mtla

Full Length Article

Refractory high entropy alloy with ductile intermetallic B2 matrix / hard bcc particles and exceptional strain hardening capacity

Nikita Yurchenko*, Evgeniya Panina, Dmitry Shaysultanov, Sergey Zherebtsov, Nikita Stepanov

Laboratory of Bulk Nanostructured Materials, Belgorod National Research University, Belgorod 308015, Russia

ARTICLE INFO

Keywords:
Refractory high entropy alloys
B2 phase
Structure
Mechanical properties
Deformation behavior

ABSTRACT

In this study, a new $Nb_{30}Mo_{30}Hf_{20}Co_{20}$ (at. %) refractory high entropy alloy (RHEA) comprising an intermetallic (Hf, Co)-rich B2 matrix and disordered (Nb, Mo)-rich bcc particles was introduced. The B2 matrix showed relatively high dislocation mobility, which, coupled with its continuity, allowed bridging and blunting of the cracks formed in the hard bcc particles during plastic deformation. The complex deformation behavior of the constitutive phases resulted in extraordinary high strain hardening capacity at 22–600 °C, exceeding single- and multi-phase RHEAs, together with the high strength. Our work endows new opportunities to develop high-performance alloys for high-temperature applications.

1. Introduction

Refractory high entropy alloys (RHEAs), introduced in the pioneering works by Senkov et al. [1,2], revived the interest in refractory metals as potential materials for next-generation gas turbine engines [3]. The firstly reported NbMoTaW and VNbMoTaW RHEAs with single-phase body-centred cubic (bcc, A2) structures outperformed the state-of-art nickel-based superalloys at T > 1000 °C and retained extraordinary strength up to 1600 °C. Later, numerous RHEAs with promising properties have been presented [4] but, among them, the so-called Refractory High Entropy SuperAlloys (RHESAs) appealed to particular attention [5–12]. These alloys usually belong to the Al-Mo-Nb-Ta-V-Ti-Zr system and comprise coherent, nanosized, cuboid bcc and B2 (ordered bcc) phases, mimicking the γ/γ' structure of nickel-based superalloys.

However, future RHESAs' development based on the aforementioned alloys' system is impeded by several key factors. Firstly, most reported RHESAs consist of the B2 matrix and embedded bcc particles (B2+bcc), resulting in high strength albeit low ductility [7,8]. An "inverted" microstructure with the bcc matrix and B2 particles (bcc+B2) ensures more balanced mechanical performance, but it is rarely observed in RHESAs and requires specific heat or thermomechanical treatment [6,8,13]. Secondly, the relatively low accuracy of the B2 phase's description, comprising Al and refractory metal(s), in relevant binaries and ternaries limits the efficiency of a CALPHAD (CALculation of PHAse Diagrams) method in the RHESAs' design [11]. Thirdly, the bcc+B2 microstructure can be unstable at temperatures of potential application: coarsening, dissolution, or disordering of (Al, Zr)-rich B2 particles and the precipitation of additional intermetallics occur at T > 600 °C [10,12,14]. Such microstructure degradation is detrimental to mechanical properties [12,15].

The present study introduces an alternative design philosophy of the bcc/B2 RHEAs. Currently, the B2 phase is considered a hard yet brittle reinforcement of the softer bcc matrix. Meanwhile, it was reported that some B2 compounds could be ductile at ambient temperature [16]. For example, polycrystalline Co-X (X = Ti, Zr, Hf) B2 phases demonstrate impressive room-temperature ductility even in tension, the positive temperature dependence of the yield stress, and exceptional strengthening during loading [17–19]. Also, high melting points, especially of the CoHf (1640 °C), make these phases attractive for high-temperature applications [20]. However, due to the relatively low yield point of the Co-X (X = Ti, Zr, Hf) intermetallics [17,21], it would be interesting to generate a dual-phase microstructure to benefit from additional strengthening mechanisms. Here, we present a new $Nb_{30}Mo_{30}Hf_{20}Co_{20}$ (at.%) RHEA with good mechanical performance thanks to a combination of ductile B2 matrix and hard bcc particles.

2. Materials and methods

A 20 g ingot of the alloy with a nominal composition of $Nb_{30}Mo_{30}Hf_{20}Co_{20}$ was produced by vacuum arc melting of pure (≥ 99.9 wt. %) elements. The phase composition and microstructure of the alloy were studied for the as-cast state using a RIGAKU diffractometer and Cu Kα radiation (XRD), an FEI Quanta 600 FEG scanning electron microscope (SEM), and JEOL JEM-2100 transmission electron microscope (TEM) equipped with an energy-dispersive (EDS) detector. Data on the actual chemical composition and impurities' content are given in Table 1.

* Corresponding author.
E-mail address: yurchenko_nikita@bsu.edu.ru (N. Yurchenko).

https://doi.org/10.1016/j.mtla.2021.101225
Received 3 July 2021; Accepted 12 September 2021
Available online 15 September 2021

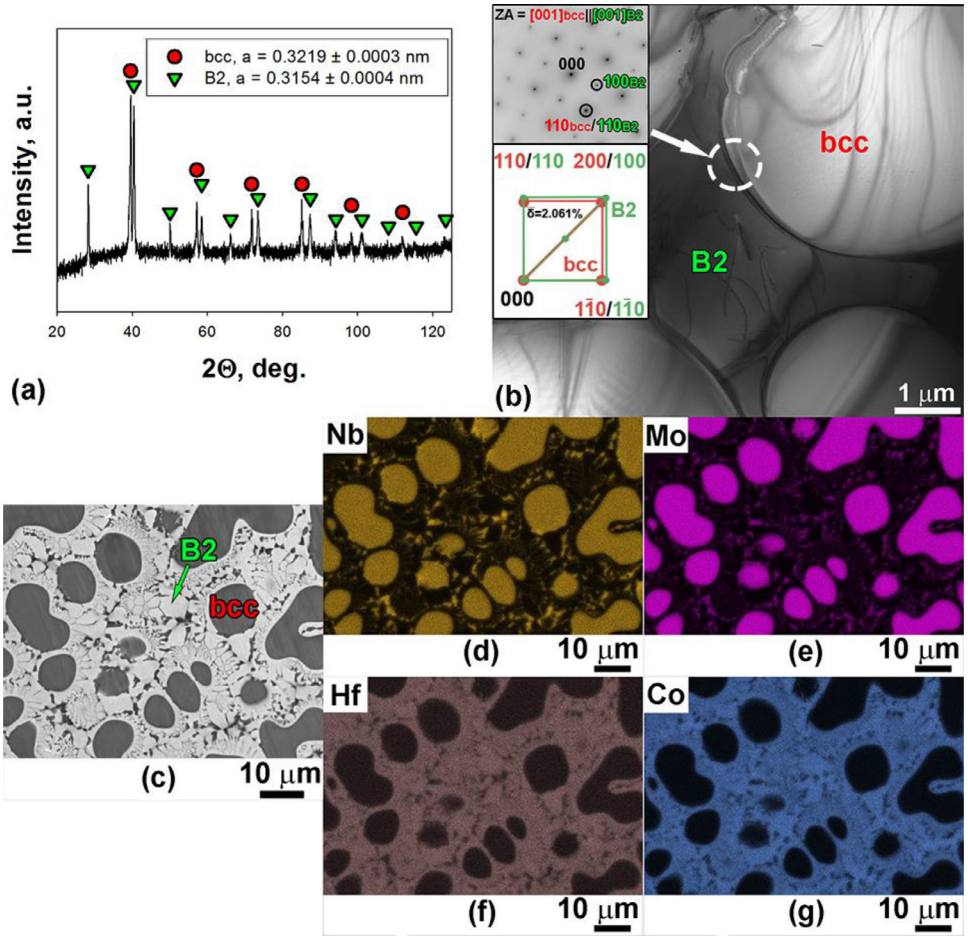

Fig. 1. As-cast structure of the $Nb_{30}Mo_{30}Hf_{20}Co_{20}$ alloy: (a) – XRD pattern with denoted Bragg's peaks and the lattice parameters of the bcc and B2 phases; (b) – TEM bright-field image with a selected area diffraction (SAED) pattern taken from the bcc/B2 interface and a schematic representation showing "cube-on-cube" $(110)_{bcc}||(110)_{B2}$, $(200)_{bcc}||(100)_{B2}$, and $(1\bar{1}0)_{bcc}||(1\bar{1}0)_{B2}$ ORs and lattice misfit, δ, between the bcc and B2 phases; (c) – SEM-BSE image illustrating a composite-like arrangement of the bcc and B2 phases; (d–g) – EDS maps presenting the distribution of Nb (d), Mo (e), Hf (f), and Co (g) among the constitutive phases.

Table 1
Actual chemical composition of the $Nb_{30}Mo_{30}Hf_{20}Co_{20}$ alloy. The actual alloy's composition given in at. % was measured by EDS analysis. The impurities' (oxygen and nitrogen) content (given in ppm) was determined by inert gas fusion.

Elements, at.%				Oxygen content, ppm	Nitrogen content, ppm
Nb	Mo	Hf	Co		
28.2 ± 0.9	30.3 ± 0.6	20.7 ± 0.7	20.8 ± 1.1	390 ± 15	30 ± 5

Table 2
Chemical composition and volume fractions of the constitutive phases of the $Nb_{30}Mo_{30}Hf_{20}Co_{20}$ alloy.

Phase	Volume fraction, %	Elements, at.%			
		Nb	Mo	Hf	Co
bcc	55 ± 2	36.0 ± 0.8	53.5 ± 2.1	8.4 ± 0.6	2.1 ± 0.7
B2	45 ± 2	7.3 ± 0.5	3.3 ± 0.4	44.0 ± 1.4	45.4 ± 1.7

The phases' volume fractions were measured by the areal analysis of SEM-BSE images using a Digimizer Image Analysis Software.

For mechanical tests, rectangular samples measured 5 × 3 × 3 mm^3 were used. The uniaxial compression tests were performed at 22, 600, 800, or 1000 °C in the air using an Instron 300LX test machine equipped with a radial furnace. The samples tested at 600, 800, or 1000 °C were placed into the preheated furnace and held for ≈10 min to equilibrate the temperature before testing. The samples' temperature was controlled by a thermocouple attached to a side surface of the specimen. The initial strain rate was 10^{-4} s^{-1}. Testing was carried out to the fracture of the specimens or to 0.6 of true strain. Two additional compression tests at 600 °C to either ~ 0.025 or ~ 0.16 of true strain were conducted. The compressed specimens were cut in half, and their structures were studied on a plane parallel to the compression axis. Note, no internal oxidation of the specimens tested in the high-temperature regime was observed.

3. Results

Fig. 1 collects XRD, TEM, and SEM-EDS data on the as-cast structure, while Table 2 summarizes the information on the chemical composition and volume fractions of constitutive phases of the $Nb_{30}Mo_{30}Hf_{20}Co_{20}$ alloy. XRD pattern contained Bragg's diffraction peaks belonging to bcc (prototype NbMo [22]) and B2 (prototype HfCo [23]) phases with close lattice parameters (Fig. 1(a)). TEM and SEM analysis coupled with EDS elemental maps revealed a composite-like microstructure (Fig. 1(b–g)), comprising predominantly round-shaped or elongated, primary and small secondary (Nb, Mo)-rich bcc particles embedded into a (Hf, Co)-rich B2 matrix (Table 2).

"Cube-on-cube" $(110)_{bcc}||(110)_{B2}$, $(200)_{bcc}||(100)_{B2}$, and $(1\bar{1}0)_{bcc}||(1\bar{1}0)_{B2}$ orientation relationships (ORs) between the bcc and B2 phases (Fig. 1(b)) were found by TEM investigations, which were consistent with previous data on bcc/B2 alloys, including refractory ones [5,12,24–26]. The obtained ORs were used for calculation of the lattice misfit ($\bar{\delta}$) as per the Bramfitt theory [27]:

$$\bar{\delta} = \sum_{i=1}^{3} \frac{\left| \left(d_{[uvw]^i_{bcc}} \cos\theta \right) - d_{[uvw]^i_{B2}} \right|}{d_{[uvw]^i_{B2}}} \times 100\ \% \quad (1)$$

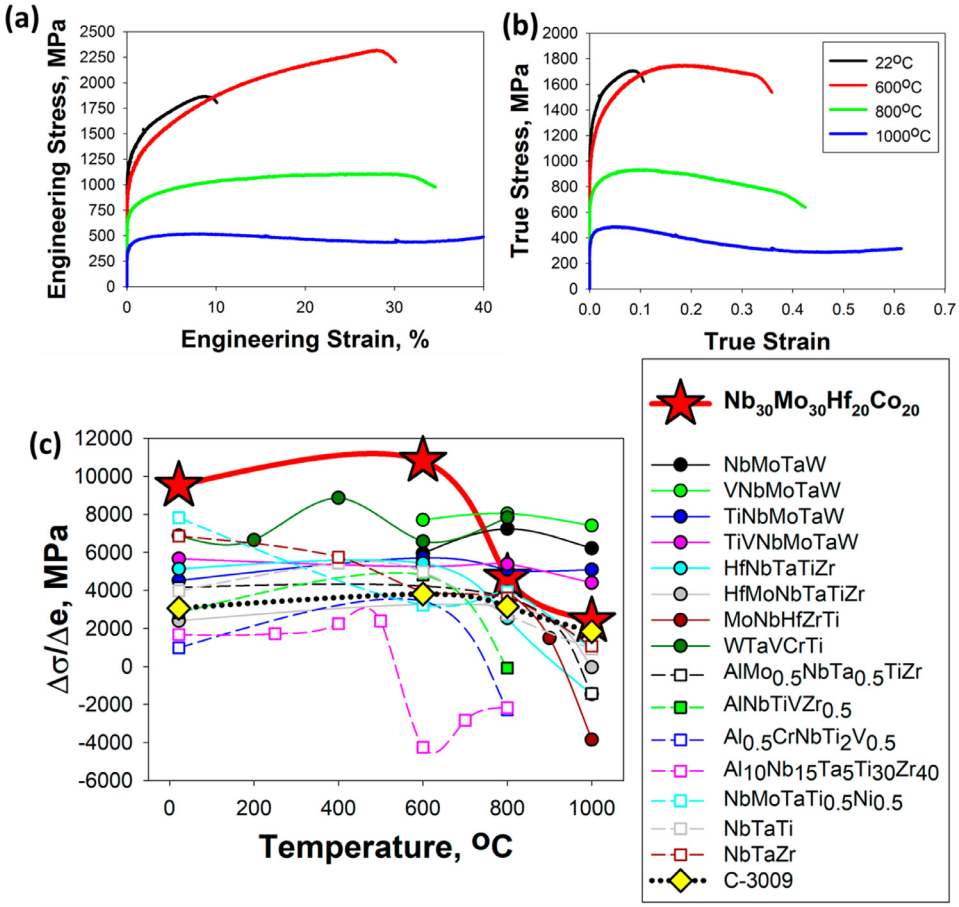

Fig. 2. (a) Engineering stress – engineering strain and (b) true stress – true strain curves of the $Nb_{30}Mo_{30}Hf_{20}Co_{20}$ alloy obtained during compression tests at 22–1000 °C; (c) Temperature dependence of strain hardening parameter, $\Delta\sigma/\Delta e$, of the $Nb_{30}Mo_{30}Hf_{20}Co_{20}$ alloy in comparison with some other RHEAs and refractory C-3009 alloy listed in Supplementary material, Table S2.

Table 3
Mechanical properties (compression yield stress (σ_y), total engineering strain (ε), true stress at 0.05 of true strain ($\sigma_{0.05}$), true peak stress (σ_p), total true strain (e), and the $\Delta\sigma/\Delta e$ parameter) of the $Nb_{30}Mo_{30}Hf_{20}Co_{20}$ alloy at 22–1000 °C.

Compression temperature,°C	σ_y, MPa	ε, %	$\sigma_{0.05}$, MPa	σ_p, MPa	e	$\Delta\sigma/\Delta e$, MPa
22	1180 ± 40	10 ± 1	1635 ± 50	1710 ± 70	0.11 ± 0.01	9479 ± 208
600	1000 ± 25	30 ± 3	1520 ± 60	1750 ± 90	0.36 ± 0.03	10833 ± 729
800	685 ± 20	35 ± 2	910 ± 35	935 ± 50	0.42 ± 0.02	4688 ± 313
1000	370 ± 20	> 40	485 ± 30	490 ± 30	> 0.5	2396 ± 208

where $[uvw]_{bcc}$ and $[uvw]_{B2}$ are Miller indices for the low-index crystal directions of bcc and B2 phases, respectively; $d_{[uvw]bcc}$ and $d_{[uvw]B2}$ are the interatomic spacing along $[uvw]_{bcc}$ and $[uvw]_{B2}$, respectively; θ is an angle between $[uvw]_{bcc}$ and $[uvw]_{B2}$. The calculation parameters are listed in Supplementary material, Table S1. According to Eq. (1), the lattice misfit between the bcc and B2 phases was found to be $\bar{\delta}$= 2.061 %, indicating a coherent nature of bcc/B2 interfaces [26,27].

Fig. 2(a) illustrates engineering stress – engineering strain curves of the as-cast $Nb_{30}Mo_{30}Hf_{20}Co_{20}$ alloy obtained during compression tests at 22–1000 °C; Table 3 assembles data on the alloy's mechanical properties. The first-look evaluation of mechanical properties revealed a conventional, negative temperature dependence of the alloy's yield stress (σ_y) accompanied by increasing total engineering strain (ε).

Meanwhile, the alloy showed a distinctive behavior after yielding. The steep and extended strain hardening stage was observed in the true stress – true strain curves at 22 and 600 °C (Fig. 2(b)). At 800–1000 °C, the alloy experienced shorter and less pronounced strengthening, followed by softening (800 °C) or softening with steady-flow stages (1000 °C) (Fig. 2(b), Table 3). We compared the temperature dependence of strain hardening parameter ($\Delta\sigma/\Delta e$) of the $Nb_{30}Mo_{30}Hf_{20}Co_{20}$ alloy and numerous single- [2,28–32] and multi-phase [15,33–37] RHEAs, and refractory C-3009 alloy [38] (Fig. 2(c), Table 3, Supplementary material, Table S2). The $\Delta\sigma/\Delta e$ parameter, calculated as $\Delta\sigma/\Delta e = (\sigma_{0.05} - \sigma_y)/(0.05–0.002)$, shows the average strain hardening rate between 0.05 of true strain and the yield point (e = 0.002). The used range seems suitable for collating the post-yielding behavior of different RHEAs and other refractory alloys in terms of room-temperature ductility and high-temperature softening resistance. The $Nb_{30}Mo_{30}Hf_{20}Co_{20}$ alloy demonstrated much higher $\Delta\sigma/\Delta e$ values (~ 10,000 MPa) in the interval of 22–600 °C in contrast to the selected counterparts. Yet, when approaching T = 800–1000 °C, the $\Delta\sigma/\Delta e$ parameter of the $Nb_{30}Mo_{30}Hf_{20}Co_{20}$ alloy declined rapidly, but it still outperformed all the multi-phase RHEAs and C-3009 alloy. Only several single-phase RHEAs, namely NbMoTaW, VNbMoTaW, TiNbMoTaW, TiVNbMoTaW, and WTaVCrTi, showed greater $\Delta\sigma/\Delta e$ values than the $Nb_{30}Mo_{30}Hf_{20}Co_{20}$ alloy. Notably, most multi-phase and some single-phase RHEAs had negative $\Delta\sigma/\Delta e$ values at T ≥ 600 °C indicating severe softening during plastic deformation.

To elucidate the nature of the unique mechanical behavior of the $Nb_{30}Mo_{30}Hf_{20}Co_{20}$ alloy, we performed a detailed investigation of the

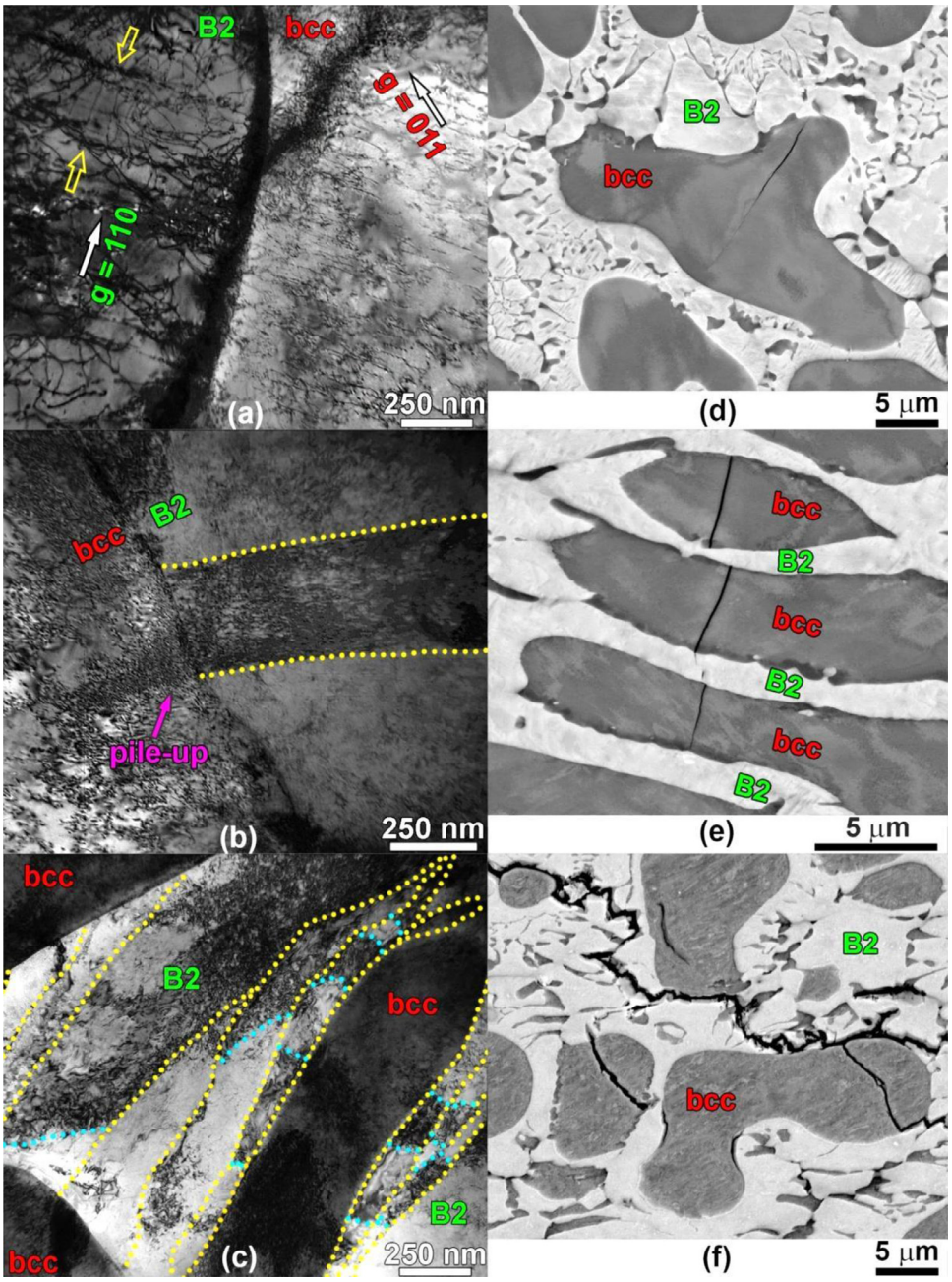

Fig. 3. Structure of the $Nb_{30}Mo_{30}Hf_{20}Co_{20}$ alloy after compression at $T = 600$ °C to $e \approx 0.025$ (a,d), 0.16 (b,e), and 0.36 (c,f): (a–c) – TEM bright-field images; (d–f) – SEM-BSE images. For SEM-BSE images, the compression axis is vertical.

microstructure evolution during compression at 600 °C (Fig. 3). After a small strain ($e \approx 0.025$), dislocation slip-mediated plastic deformation was developed within both the bcc and B2 phases (Fig. 3(a)). In contrast to straight and randomly distributed mixed-type dislocations in the bcc phase, a more complex dislocation arrangement was found in the B2 phase. Multiple dislocations tended to form parallel dislocation walls (DWs) located mostly perpendicular to the bcc/B2 interfaces (shown by yellow arrows). Between these DWs, sporadic dislocation pile-ups and individual dislocations were observed (Fig. 3(a)).

At a higher strain ($e \approx 0.16$) closely corresponded to the true peak stress (Fig. 3(b)), the formation of bands/lamellae (denoted with yellow dotted lines) containing high dislocations density was observed inside the B2 phase. In the bcc phase, the pile-ups accumulation near the bcc/B2 interfaces (denoted with pink arrow) adjusted to the bands/lamellae location in the B2 phase should be noted. At the fracture strain ($e = 0.36$) (Fig. 3(c)), transversal boundaries (denoted with bright blue dotted lines) were found within individual B2 bands/lamellae. Meantime, dislocation tangles/pile-ups inside the bcc phase propagated from one interphase boundary to another.

On the macroscopic level, the early deformation stage was accompanied by the nucleation of individual cracks inside the bcc particles near the bcc/B2 interfaces (Fig. 3(d)). Further straining to $e \approx 0.16$ led to bridging, deflection, and blunting by the B2 phase of the cracks propagated through the entire volume of the bcc particles (Fig. 3(e)). Analysis of the specimen's cross-section after fracture ($e = 0.36$), slightly away from the fracture surface, revealed the dominated cracking along the bcc/B2 interfaces coupled with the multiple secondary cracking of the bcc particles (Fig. 3(f)). Note, the B2 matrix, in the area of view, remained almost free of cracks. Besides, no other than the B2 and bcc phases appeared after plastic deformation at 600 °C (Fig. 3(f)) and 800 °C (Supplementary material, Fig. S1), suggesting relatively high phase stability of the $Nb_{30}Mo_{30}Hf_{20}Co_{20}$ alloy.

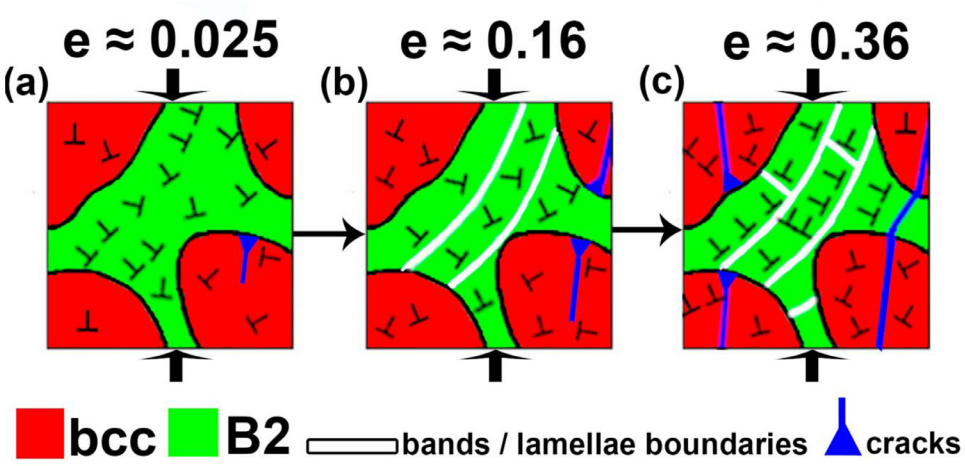

Fig. 4. Scheme showing the microstructure evolution of the $Nb_{30}Mo_{30}Hf_{20}Co_{20}$ alloy during compression at 600 °C to different plastic strains.

4. Discussion

One of the most interesting findings of our study is the exceptional strain hardening capacity of the $Nb_{30}Mo_{30}Hf_{20}Co_{20}$ alloy at 22–600 °C (Fig. 2). The origin of the unusual mechanical behavior stems from the alloy's structure, which can be rationalized by the CALPHAD (Supplementary material, Fig. S2). Thermodynamic modelling predicts the separation of (Nb, Mo)-rich and (Hf, Co)-rich liquids, further solidifying through the bcc and B2 phases, respectively. Liquid phase separation (LPS) is a common phenomenon in HEAs that induces a composite-like structure formation [39]. Traditionally, LPS results from the elements with positive mixing enthalpy [40], but a recent study shows the occurrence of LPS due to higher negative mixing enthalpy between some components [41]. It can be speculated that the $Nb_{30}Mo_{30}Hf_{20}Co_{20}$ alloy combines both features leading to LPS. Indeed, Nb and Hf are a sole pair having repulsive interaction, while Hf and Co demonstrate the highest affinity to each other (Supplementary material, Table S3). Such a complex interplay between the constitutive elements can create the liquid miscibility gap, alleviating the crystallization of the refractory (Nb, Mo)-rich bcc particles. In turn, due to low $\bar{\delta}$, the bcc particles are expected to act as effective sites [27] for heterogeneous nucleation of the continuous (Hf, Co)-rich B2 phase with a temperature decrease. It should also be noted that the CALPHAD gives accurate qualitative and quantitative predictions of the $Nb_{30}Mo_{30}Hf_{20}Co_{20}$ alloy's phase composition, demonstrating the potential applicability of this method to search for new alloys with tailored bcc/B2 phase fractions' ratio.

Most multi-phase RHEAs show a sharp strain hardening-softening "hump" in the stress-strain curve after yielding during high-temperature deformation [7,13,15,33–37,42,43], indicating the thermal activation of plastic deformation in the hard phase, the occurrence of dynamic recrystallization, and/or phase transformations [7,13,15,42,43]. In the $Nb_{30}Mo_{30}Hf_{20}Co_{20}$ alloy, the deformation behavior at 600 °C is different. Both phases start to deform simultaneously after the yield point, but the B2 matrix demonstrates higher dislocation mobility than the bcc particles (Fig. 4(a)). Relatively ease dislocation slip in the B2 phase leads to an intensive bands/lamella formation, accompanied by constant dislocation multiplication, with a strain increment (Fig. 4(b,c)). This allows for accommodating large plastic deformation without compromising strain hardening. Meantime, the confined dislocation rearrangement within the bcc particles results in the pile-ups accumulation near the bcc/B2 interfaces, contributing to the further rising of long-range stress fields and, simultaneously, to inevitable cracking (Fig. 4(a,b)). The continuous nature of the B2 phase helps bridge and blunt the cracks [44], extending the strain hardening stage. However, although the bcc and B2 phase have a good crystallographic match (Fig. 1(b)), maintaining strain compatibility between them is problematic at large strains because of different hardness and elastic moduli (Supplementary material, Fig. S3). Note, even in this case, the B2 matrix can deflect the cracks to some extent. It should also be mentioned that the bcc particles' cracking could hardly be associated with the contamination during the high-temperature test in air, as the oxygen (502 ± 35 ppm) and nitrogen (47 ± 20 ppm) contents of the specimens compressed at 600 °C were comparable with initial ones (Table 1).

The anomalous ductility of the Co-X (Ti, Zr, Hf) B2 phases is not surprising but still argued [19]. Being highly ordered compounds, they show primary <100> slip mode, not satisfying the well-known von Mises criterion required five independent slip systems [45]. Particularly, Yoshida and Takasugi [46] reported that plastic deformation in the CoHf compound at 22–800 °C was dominated by the glide of <100> dislocations. Meantime, recent studies on CoTi and CoZr B2 phases demonstrated the possibility of "hard" <011> or <111> slip modes at higher strains [21,47], thus providing a plausible explanation for the inherent ductility of these intermetallics. To clarify this moment in the case of the $Nb_{30}Mo_{30}Hf_{20}Co_{20}$ alloy, we performed a more detailed TEM analysis after compression to $e \approx 0.025$ (Supplementary material, Fig. S4) and revealed the presence of numerous dislocations with <011> or/and <111> Burgers vectors in the B2 matrix. Activating such "hard" slip modes can stem from the relaxation of long-range back-stresses [19] caused by the rigid bcc particles. In turn, supersaturation with Nb and Mo (Table 2) is assumed to be another reason for the invoking of <011> or/and <111> dislocations. It can be speculated that Nb and Mo atoms change the lattice anisotropy, thereby equalizing the elastic strain energy for primary <100> and secondary <111> (or <011>) slip. However, further in-depth studies are highly needed to elucidate the fundamentals of the B2 phase' ductility.

To put the obtained results in a broader context, "soft solid solution matrix with hard intermetallic precipitates" is a common design philosophy for high-performance metallic alloys [48]. The current study, however, revealed that a combination of a ductile intermetallic matrix with hard disordered reinforcements could also be a viable option, especially for high-temperature materials. Moreover, the vast compositional space of HEAs allows adjusting of the properties of both intermetallic matrix and disordered particles. For example, recent studies have demonstrated how the elemental distribution and short-range order can be tailored to improve the mechanical behavior of fcc HEAs [49,50]. Also, superior mechanical properties of a precipitation-hardened HEA were ascribed to multicomponent nanoparticles combining strength and ductility [51]. Given the enormous number of possible B2 compounds and their homogeneity range in multicomponent alloys [11], the characteristics of the B2 matrix can likely be modified to get a required strength-ductility balance. Proper alloying and (probably) processing are expected to provide an optimal amount and distribution of the strengthening phases,

thus opening another option to control the mechanical performance of future (R)HEAs with the B2 matrix.

5. Conclusion

In summary, we introduced the $Nb_{30}Mo_{30}Hf_{20}Co_{20}$ alloy with the composite-like microstructure consisting of the ordered (Hf, Co)-rich B2 matrix and disordered (Nb, Mo)-rich bcc particles. The alloy showed outstanding strain hardening capacity at 22–600 °C, surpassing the currently reported refractory high entropy alloys. The decent mechanical performance of the alloy stemmed from the much higher ductility of the intermetallic B2 matrix than the disordered bcc particles. Ease dislocation glide and deformation-induced substructure formation with continuous dislocation multiplication in the B2 matrix together with its continuity confined the cracking of the hard bcc particles, thus preventing premature fracture and promoting strain hardening stage. This study alters the traditional roles of disordered (matrix) and ordered (particles) phases in precipitation-strengthened metallic alloys developed for high-temperature applications.

Declaration of Competing Interest

The authors declare that they have no known competing financial interests or personal relationships that could have appeared to influence the work reported in this paper.

Acknowledgments

The authors gratefully acknowledge the financial support from the Russian Science Foundation Grant no. 19-79-30066. The authors are grateful to the personnel of the Joint Research Center, "Technology and Materials", Belgorod National Research University, for their assistance. The authors also thank Dr. A Belyakov, Belgorod National Research University, for fruitful discussions.

Supplementary materials

Supplementary material associated with this article can be found, in the online version, at doi:10.1016/j.mtla.2021.101225.

References

[1] O.N. Senkov, G.B. Wilks, D.B. Miracle, C.P. Chuang, P.K. Liaw, Refractory high-entropy alloys, Intermetallics 18 (2010) 1758–1765, doi:10.1016/j.intermet.2010.05.014.

[2] O.N. Senkov, G.B. Wilks, J.M. Scott, D.B. Miracle, Mechanical properties of $Nb_{25}Mo_{25}Ta_{25}W_{25}$ and $V_{20}Nb_{20}Mo_{20}Ta_{20}W_{20}$ refractory high entropy alloys, Intermetallics 19 (2011) 698–706, doi:10.1016/j.intermet.2011.01.004.

[3] E. Pink, R. Eck, Refractory metals and their alloys, Mater. Sci. Technol. (2006), doi:10.1002/9783527603978.mst0088.

[4] O.N. Senkov, D.B. Miracle, K.J. Chaput, J.P. Couzinie, Development and exploration of refractory high entropy alloys - a review, J. Mater. Res. 33 (2018) 3092–3128, doi:10.1557/jmr.2018.153.

[5] O.N. Senkov, D. Isheim, D.N. Seidman, A.L. Pilchak, Development of a refractory high entropy superalloy, Entropy 18 (2016) 1–13, doi:10.3390/e18030102.

[6] V. Soni, O.N. Senkov, B. Gwalani, D.B. Miracle, R. Banerjee, Microstructural design for improving ductility of an initially brittle refractory high entropy alloy, Sci. Rep. (2018) 1–10, doi:10.1038/s41598-018-27144-3.

[7] O.N. Senkov, S. Rao, K.J. Chaput, C. Woodward, Compositional effect on microstructure and properties of NbTiZr-based complex concentrated alloys, Acta Mater. 151 (2018) 201–215, doi:10.1016/j.actamat.2018.03.065.

[8] D. Schliephake, A.E. Medvedev, M.K. Imran, S. Obert, D. Fabijanic, M. Heilmaier, A. Molotnikov, X. Wu, Precipitation behavior and mechanical properties of a novel Al0.5MoTaTi complex concentrated alloy, Scr. Mater. 173 (2019) 16–20, doi:10.1016/J.SCRIPTAMAT.2019.07.033.

[9] V. Soni, O.N. Senkov, J.-P. Couzinie, Y. Zheng, B. Gwalani, R. Banerjee, Phase stability and microstructure evolution in a ductile refractory high entropy alloy Al10Nb15Ta5Ti30Zr40, Materialia 9 (2020) 100569, doi:10.1016/j.mtla.2019.100569.

[10] T.E. Whitfield, E.J. Pickering, L.R. Owen, C.N. Jones, H.J. Stone, N.G. Jones, The effect of Al on the formation and stability of a BCC – B2 microstructure in a refractory metal high entropy superalloy system, Materialia 13 (2020) 100858, doi:10.1016/j.mtla.2020.100858.

[11] D.B. Miracle, M.H. Tsai, O.N. Senkov, V. Soni, R. Banerjee, Refractory high entropy superalloys (RSAs), Scr. Mater. 187 (2020) 445–452, doi:10.1016/j.scriptamat.2020.06.048.

[12] Q. Wang, J. Han, Y. Liu, Z. Zhang, C. Dong, P.K. Liaw, Coherent precipitation and stability of cuboidal nanoparticles in body-centered-cubic Al0.4Nb0.5Ta0.5TiZr0.8 refractory high entropy alloy, Scr. Mater. 190 (2021) 40–45, doi:10.1016/j.scriptamat.2020.08.029.

[13] O.N. Senkov, J.K. Jensen, A.L. Pilchak, D.B. Miracle, H.L. Fraser, Compositional variation effects on the microstructure and properties of a refractory high-entropy superalloy AlMo0.5NbTa0.5TiZr, Mater. Des. 139 (2018) 498–511, doi:10.1016/j.matdes.2017.11.033.

[14] V. Soni, B. Gwalani, O.N. Senkov, B. Viswanathan, T. Alam, D.B. Miracle, R. Banerjee, Phase stability as a function of temperature in a refractory high-entropy alloy, J. Mater. Res. 33 (2018) 3235–3246, doi:10.1557/jmr.2018.223.

[15] O.N. Senkov, J.-P. Couzinie, S.I. Rao, V. Soni, R. Banerjee, Temperature dependent deformation behavior and strengthening mechanisms in a low density refractory high entropy alloy Al10Nb15Ta5Ti30Zr40, Materialia (2020) 100627, doi:10.1016/j.mtla.2020.100627.

[16] K. Gschneidner, A. Russell, A. Pecharsky, J. Morris, Z. Zhang, T. Lograsso, D. Hsu, C.H.C. Lo, Y. Ye, A. Slager, D. Kesse, A family of ductile intermetallic compounds, Nat. Mater. 2 (2003) 587–590, doi:10.1038/nmat958.

[17] T. Takasugi, O. Izumi, M. Yoshida, Anomalous temperature dependence of the yield strength in IVa-VIII intermetallic compounds with B_2 structure, J. Mater. Sci. 26 (1991) 2941–2948, doi:10.1007/BF01124825.

[18] T. Yamaguchi, Y. Kaneno, T. Takasugi, Room-temperature tensile property and fracture behavior of recrystallized B2-type CoZr intermetallic compound, Scr. Mater. 52 (2005) 39–44, doi:10.1016/j.scriptamat.2004.09.002.

[19] S.R. Agnew, T. Ungar, Determination of the dislocation-based mechanism(s) responsible for the anomalous ductility of a class of B2 intermetallic alloys, IOP Conf. Ser. Mater. Sci. Eng. (2019) 580, doi:10.1088/1757-899X/580/1/012001.

[20] D.L. Anton, D.M. Shah, D.N. Duhl, A.F. Giamei, Selecting high-temperature structural intermetallic compounds: the engineering approach, JOM 41 (1989) 12–17, doi:10.1007/BF03220324.

[21] J.A. Wollmershauser, C.J. Neil, S.R. Agnew, Mechanisms of ductility in CoTi and CoZr B2 intermetallics, Metall. Mater. Trans. A Phys. Metall. Mater. Sci. 41 (2010) 1217–1229, doi:10.1007/s11661-009-9990-2.

[22] W.C. Hubbell, F.R. Brotzen, Elastic constants of niobium-molybdenum alloys in the temperature range -190 to +100°C, J. Appl. Phys. 43 (1972) 3306–3312, doi:10.1063/1.1661712.

[23] R.M. Van Essen, K.H.J. Buschow, Hydrogen absorption in various zirconium-and hafnium-based intermetallic compounds, J. Less Common Met. 64 (1979) 277.

[24] G. Ghosh, G.B. Olson, Integrated design of Nb-based superalloys: Ab initio calculations, computational thermodynamics and kinetics, and experimental results, Acta Mater. 55 (2007) 3281–3303, doi:10.1016/j.actamat.2007.01.036.

[25] A.J. Knowles, D. Dye, R.J. Dodds, A. Watson, C.D. Hardie, S.A. Humphry-Baker, Tungsten-based bcc-superalloys, Appl. Mater. Today 23 (2021) 101014, doi:10.1016/j.apmt.2021.101014.

[26] C. Yang, L.M. Kang, X.X. Li, W.W. Zhang, D.T. Zhang, Z.Q. Fu, Y.Y. Li, L.C. Zhang, E.J. Lavernia, Bimodal titanium alloys with ultrafine lamellar eutectic structure fabricated by semi-solid sintering, Acta Mater. 132 (2017) 491–502, doi:10.1016/j.actamat.2017.04.062.

[27] B.L. Bramfitt, The effect of carbide and nitride additions on the heterogeneous nucleation behavior of liquid iron, Metall. Trans. 1 (1970) 2958, doi:10.1007/BF03037838.

[28] Z.D. Han, N. Chen, S.F. Zhao, L.W. Fan, G.N. Yang, Y. Shao, K.F. Yao, Effect of Ti additions on mechanical properties of NbMoTaW and VNbMoTaW refractory high entropy alloys, Intermetallics 84 (2017) 153–157, doi:10.1016/J.INTERMET.2017.01.007.

[29] O.N. Senkov, J.M. Scott, S.V. Senkova, F. Meisenkothen, D.B. Miracle, C.F. Woodward, Microstructure and elevated temperature properties of a refractory TaNbHfZrTi alloy, J. Mater. Sci. 47 (2012) 4062–4074, doi:10.1007/s10853-012-6260-2.

[30] C.-C. Juan, M.-H. Tsai, C.-W. Tsai, C.-M. Lin, W.-R. Wang, C.-C. Yang, S.-K. Chen, S.-J. Lin, J.-W. Yeh, Enhanced mechanical properties of HfMoTaTiZr and HfMoNbTaTiZr refractory high-entropy alloys, Intermetallics 62 (2015) 76–83, doi:10.1016/J.INTERMET.2015.03.013.

[31] N.N. Guo, L. Wang, L.S. Luo, X.Z. Li, Y.Q. Su, J.J. Guo, H.Z. Fu, Microstructure and mechanical properties of refractory MoNbHfZrTi high-entropy alloy, Mater. Des. 81 (2015) 87–94, doi:10.1016/J.MATDES.2015.05.019.

[32] I.H. Kim, H.S. Oh, K.S. Lee, E.S. Park, Optimization of conflicting properties via engineering compositional complexity in refractory high entropy alloys, Scr. Mater. 199 (2021) 113839, doi:10.1016/j.scriptamat.2021.113839.

[33] O.N. Senkov, C. Woodward, D.B. Miracle, Microstructure and properties of aluminum-containing refractory high-entropy alloys, JOM 66 (2014) 2030–2042, doi:10.1007/s11837-014-1066-0.

[34] N.Y. Yurchenko, N.D. Stepanov, S.V. Zherebtsov, M.A. Tikhonovsky, G.A. Salishchev, Structure and mechanical properties of B2 ordered refractory AlNbTiVZrx (x = 0–1.5) high-entropy alloys, Mater. Sci. Eng. A 704 (2017) 82–90, doi:10.1016/j.msea.2017.08.019.

[35] N.D. Stepanov, N.Y. Yurchenko, E.S. Panina, M.A. Tikhonovsky, S.V. Zherebtsov, Precipitation-strengthened refractory $Al_{0.5}CrNbTi_2V_{0.5}$ high entropy alloy, Mater. Lett. 188 (2017) 162–164, doi:10.1016/J.MATLET.2016.11.030.

[36] H. Zhang, Y. Zhao, J. Cai, S. Ji, J. Geng, X. Sun, D. Li, High-strength NbMoTaX refractory high-entropy alloy with low stacking fault energy eutectic phase via laser additive manufacturing, Mater. Des. 201 (2021) 109462, doi:10.1016/j.matdes.2021.109462.

[37] O.N. Senkov, J. Gild, T.M. Butler, Microstructure, mechanical properties and oxidation behavior of NbTaTi and NbTaZr refractory alloys, J. Alloys Compd. 862 (2021) 158003, doi:10.1016/J.JALLCOM.2020.158003.
[38] O.N. Senkov, S.I. Rao, T.M. Butler, T.I. Daboiku, K.J. Chaput, Microstructure and properties of Nb-Mo-Zr based refractory alloys, Int. J. Refract. Met. Hard Mater. 92 (2020) 105321, doi:10.1016/J.IJRMHM.2020.105321.
[39] N. Derimow, R. Abbaschian, Liquid phase separation in high-entropy alloys-a review, Entropy 20 (2018) 890, doi:10.3390/e20110890.
[40] T. Nagase, M. Todai, T. Nakano, Development of Ti–Zr–Hf–Y–La high-entropy alloys with dual hexagonal-close-packed structure, Scr. Mater. 186 (2020) 242–246, doi:10.1016/j.scriptamat.2020.05.033.
[41] A. Munitz, I. Edry, E. Brosh, N. Derimow, B.E. MacDonald, E.J. Lavernia, R. Abbaschian, Liquid phase separation in $AlCrFeNiMo_{0.3}$ high-entropy alloy, Intermetallics 112 (2019) 106517, doi:10.1016/j.intermet.2019.106517.
[42] N.D. Stepanov, N.Y. Yurchenko, D.V. Skibin, M.A. Tikhonovsky, G.A. Salishchev, Structure and mechanical properties of the AlCrxNbTiV (x = 0, 0.5, 1, 1.5) high entropy alloys, J. Alloys Compd. 652 (2015) 266–280, doi:10.1016/j.jallcom.2015.08.224.
[43] N. Yurchenko, E. Panina, S. Zherebtsov, N. Stepanov, Design and characterization of eutectic refractory high entropy alloys, Materialia 16 (2021) 101057, doi:10.1016/j.mtla.2021.101057.
[44] R.D. Noebe, F.J. Ritzert, A. Misra, R. Gibala, Prospects for ductility and toughness enhancement of NiAI by ductile phase reinforcement, (1991). https://ntrs.nasa.gov/search.jsp?R=19910018010.
[45] R.V. Mises, Mechanik der plastischen Formänderung von kristallen, ZAMM J. Appl. Math. Mech. Zeitschrift Für Angew. Math. Und Mech 8 (1928) 161–185, doi:10.1002/zamm.19280080302.
[46] M. Yoshida, T. Takasugi, Transmission electron microscopy study of the activated slip systems and the dislocation structures in B2-type CoZr and CoHf polycrystals, Philos. Mag. A Phys. Condens. Matter Struct. Defects Mech. Prop 68 (1993) 401–417, doi:10.1080/01418619308221212.
[47] R.P. Mulay, S.R. Agnew, Hard slip mechanisms in B2 CoTi, Acta Mater. 60 (2012) 1784–1794, doi:10.1016/j.actamat.2011.11.061.
[48] D.B. Miracle, Critical assessment: critical assessment 14: high entropy alloys and their development as structural materials, Mater. Sci. Technol. 31 (2015) 1142–1147 (United Kingdom), doi:10.1179/1743284714Y.0000000749.
[49] Q. Ding, Y. Zhang, X. Chen, X. Fu, D. Chen, S. Chen, L. Gu, F. Wei, H. Bei, Y. Gao, M. Wen, J. Li, Z. Zhang, T. Zhu, R.O. Ritchie, Q. Yu, Tuning element distribution, structure and properties by composition in high-entropy alloys, Nature 574 (2019) 223–227, doi:10.1038/s41586-019-1617-1.
[50] R. Zhang, S. Zhao, J. Ding, Y. Chong, T. Jia, C. Ophus, M. Asta, R.O. Ritchie, A.M. Minor, Short-range order and its impact on the CrCoNi medium-entropy alloy, Nature 581 (2020) 283–287, doi:10.1038/s41586-020-2275-z.
[51] T. Yang, Y.L. Zhao, Y. Tong, Z.B. Jiao, J. Wei, J.X. Cai, X.D. Han, D. Chen, A. Hu, J.J. Kai, K. Lu, Y. Liu, C.T. Liu, Multicomponent intermetallic nanoparticles and superb mechanical behaviors of complex alloys, Science 362 (2018) 933–937 (80-.), doi:10.1126/science.aas8815.